Soft-x-ray emission dynamics in picosecond laser-produced plasmas

L. A. Gizzi and A. Giulietti
Istituto di Fisica Atomica e Molecolare, Area della Ricerca del CNR, 56010 Ghezzano, Pisa, Italy

O. Willi
The Blackett Laboratory, Imperial College, London SW7 2BZ, United Kingdom

D. Riley
Department of Physics, The Queen's University of Belfast, Belfast BT7 1NN, Northern Ireland

Plasmas were generated by prepulse-free picosecond laser irradiation of solid targets consisting of five different fluorine salts. Picosecond-time-resolved x-ray spectroscopy of K-shell emission from H-like and He-like fluorine was performed to study the temporal evolution of plasma parameters including electron density and temperature. Measurements show that the fluorine line emission intensity reaches its maximum in a time comparable with the rise time of the laser pulse. This peak is then followed by a decay whose rate depends upon the atomic number of the alkali component of the target. Our measurements show clear evidence of radiation cooling effects in higher-Z targets.

PACS number(s): 52.25.Nr, 52.50.Jm, 52.70.−m

I. INTRODUCTION

The interaction of high-intensity picosecond laser plasmas with solid targets generates hot, high density, rapidly evolving plasmas. Due to the short pulse length compared with the typical plasma expansion time scale, plasma densities as high as $10^{23} e/\text{cm}^3$ can be achieved at temperatures up to 1 keV. Such plasmas exhibit suitable conditions for the generation of efficient, picosecond incoherent x-ray emission [1–3]. Hot, solid density plasmas are also characterized by a rapid cooling that can yield population inversion between levels with different principal quantum numbers ($\Delta n = 1,2$), setting the appropriate conditions for a highly efficient lasing action in the soft-x-ray region [4].

A crucial issue in the recombination x-ray laser scheme is the plasma cooling rate that determines the degree of population inversion and, consequently, the gain that can be finally achieved. Several factors can contribute to determine the cooling rate including the geometry of plasma expansion, heat transport processes, and the rate of radiation losses. Great attention has been devoted in recent years to the study of absorption processes to fully understand the mechanisms that lead to transfer of laser energy to short-scale-length plasmas.

Measurements [5–7] on absorption processes and thermal transport performed in experimental conditions similar to those reported in this paper have already shown that, in the case of normal incidence, inverse bremsstrahlung (IB) is the most efficient absorption mechanism. In the case of oblique incidence and P polarization, resonance absorption takes place in a 10-μm-scale-length density gradient and becomes competitive with IB, leading to an increase in the absorption efficiency of up to 20% [5]. By using time-resolved spectroscopy, plasmas were characterized in terms of electron temperature and density [6]. Moreover, a detailed study of thermal transport carried out in this regime has shown [7] that numerical models based on classical heat transport fail to describe the observed behavior when the absorbed laser intensity is greater than 10^{15} W/cm^2, while, for lower intensities, a flux limit of the order of 10% is needed to obtain a satisfactory agreement between theory and experiment. Even though some discrepancies still remain, the fundamental parameters governing absorption processes in the picosecond regime are well identified.

In contrast, the dynamics of subsequent processes, including radiation emission dynamics and plasma cooling, are still open issues which require large effort in terms of experimental investigation as well as theoretical and computational analysis [8]. In a previous experimental investigation [9] the temporal behavior of x-ray line emission from picosecond plasmas was studied as a function of the plasma density scale length. In that experiment the duration of the K-shell line emission from H-like and He-like carbon was found to increase strongly with the plasma scale length. This effect was explained as due to a shift of the heat deposition layer to smaller densities for longer density scale lengths.

Here we focus our investigation on the effect of a different atomic number environment on the radiative properties of a plasma. Targets consisting of different fluorine salts of increasing mean atomic number were irradiated with a prepulse-free picosecond pulse. Picosecond-time-resolved spectroscopy was used to study the temporal evolution of resonance line emission from highly ionized fluorine ions over a long (compared to the laser pulse length) time scale.

II. EXPERIMENTAL SETUP

The experiment was carried out at the Central Laser Facility of the Rutherford Appleton Laboratory using the 12 ps, 0.268 μm SPRITE laser system [10]. A schematic view of the experimental setup is shown in Fig. 1. The laser beam was focused by an off-axis parabola at a fixed intensity of 10^{15} W/cm^2 on solid targets consisting of five different fluorine salts, namely, LiF, NaF, MgF$_2$, CaF$_2$, and SrF$_2$. The
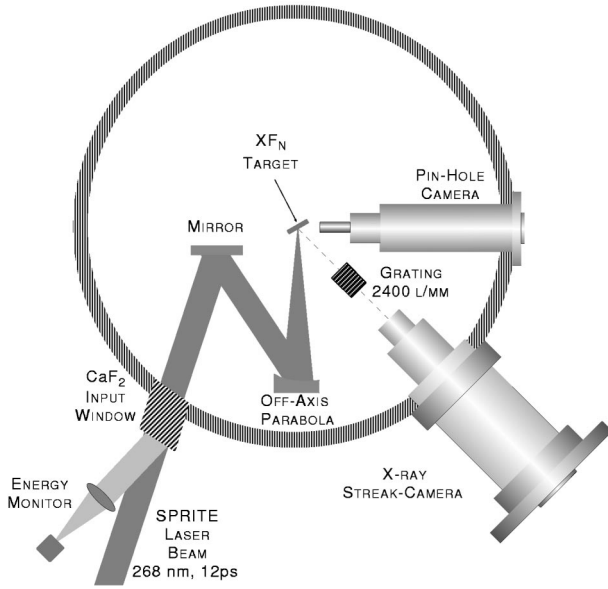
FIG. 1. Experimental setup of the interaction chamber for time-resolved soft-x-ray spectroscopy of picosecond plasmas. The plasma was generated by the interaction of a high-contrast, 12 ps, 268 nm laser pulse with solid targets consisting of fluorine salts (XF_N). The laser beam was focused on the target by means of an off-axis parabola at an intensity of 10^{15} W/cm^2 in a 30-μm diam focal spot.

spot on the target was enlarged to 3 times the best focus by placing the focusing optics slightly closer to the target. The resulting diameter of the focal spot containing 90% of the total energy was 30 μm. This enabled the interaction intensity to be sufficiently low to ensure that collisional absorption was not affected [11] by nonlinear processes. A larger focal spot has also the additional advantage of producing a more planar expansion which makes the interaction physics and the plasma evolution closer to a one-dimensional behavior, a regime which can be more easily described by numerical simulations. Also, a larger interaction area means a bigger plasmas with consequent brighter emission, an advantage from the experimental viewpoint. Finally, the angle of incidence was set to be 10° to maximize energy transfer to the plasma by resonance absorption [6].

A very important feature of our experiment is the extremely high contrast (pulse-to-prepulse intensity ratio) of the laser pulse used to irradiate the target. In fact, the laser pulse used in our experiment was basically free from the so-called prepulse consisting of a spurious laser radiation arising from amplified spontaneous emission (ASE) in the amplifier chain which can give rise to a precursor plasma formation. The contrast was measured to be greater than 10^{10}, which is orders of magnitude greater than the contrast ratios typically available with high-power lasers. In particular, this value is also much higher than the contrast achievable with ultrashort pulses based on chirped pulse amplification [12]. This is a fundamental condition to be fulfilled if short-scale-length high-density plasmas are to be generated [13]. In fact, the high contrast ensures that no premature breakdown on the target occurs and that the main pulse interacts directly with the solid target rather than with the low-density plasma generated by the prepulse. The plasma scale

length is therefore uniquely determined by the features of the main laser pulse. In our case the scale length has been accurately measured by absorption measurements as reported in [6] and was found to be 10μm.

The x-ray radiation emitted by the plasma was analyzed by means of a spectrometer equipped with a flat-field grazing incidence grating [14]. The spectrometer, set to detect K-shell line emission from He-like and H-like fluorine ions, was coupled to an x-ray streak camera that enabled the spectrum to be resolved in time with a temporal resolution of 6 ps. The overall spectral resolution was 0.5 Å and was mainly limited by the spatial resolution of the photocathode of the streak camera. A pinhole camera equipped with a 10 μm pinhole and a 30-μm-thick beryllium filter was also used to monitor the focusing conditions. According to the pinhole camera images, the size of the x-ray emitting region was typically 35 μm in diameter, a value consistent with the measured focal spot on the target.

III. EXPERIMENTAL RESULTS

Time-resolved spectra obtained from laser irradiation of LiF, NaF, MgF$_2$, CaF$_2$, and SrF$_2$ are shown in Fig. 2. Emission lines from He-like fluorine, namely, F-He$_\alpha$ ($1s^2$-$1s2p$) at 16.8 Å, and from H-like fluorine, namely, F-Ly$_\alpha$ ($1s$-$2p$) at 15.0 Å and F-Lyβ ($1s$-$3p$) at 12.6 Å, are clearly visible. Since the detailed structure of these lines is not fully resolved by our spectrometer, the lines labeled as Ly$_\alpha$ and He$_\alpha$ may also include unresolved satellites, such as dielectronic satellites. In fact, the resolution of our spectrometer is in principle sufficient to detect such satellites as a broadening of unresolved resonance lines. However, since no appreciable broadening could be found in the spectra of Fig. 2, the measured line intensity should be attributed entirely to transitions from $n=2$ to the ground state. The dip in the short-wavelength edge of the spectra is a mark on the streak-camera photocathode which acts as a wavelength fiducial. The lines are superimposed to a background consisting of a continuum emission due to bremsstrahlung and recombination.

Continuum emission intensity decays rapidly after the laser pulse. In fact, this kind of radiation is generated by the hot, high-density plasma produced during the interaction process when temperatures as high as a few hundreds of eV can be reached in the supercritical plasma region (where the electron density is greater than the critical density, $n_c=1.6 \times 10^{22}$ cm^{-3}) beyond the laser absorption layer. As the laser pulse tails off, these conditions are rapidly lost, bremsstrahlung emission quickly vanishes, and only resonance line emission remains visible for a much longer time. Such a behavior has also been observed in high temporal and spectral resolution x-ray measurements performed on Al plasmas generated under similar experimental conditions [5].

As the mean atomic number of the target increases, the underlying continuum emission becomes more intense. This is a consequence of the dependence of the bremsstrahlung emission efficiency upon the mean charge state of the plasma. Also, additional lines appear in the observed spectral region as in the case of NaF where Na-He$_\alpha$ ($1s^2$-$1s2p$) at 11 Å and Na-Ly$_\alpha$ ($1s$-$2p$) at 10 Å, which are visible on the *blue* side of fluorine lines. The Mg-He$_\alpha$ ($1s^2$-$1s2p$) at 9.2 Å
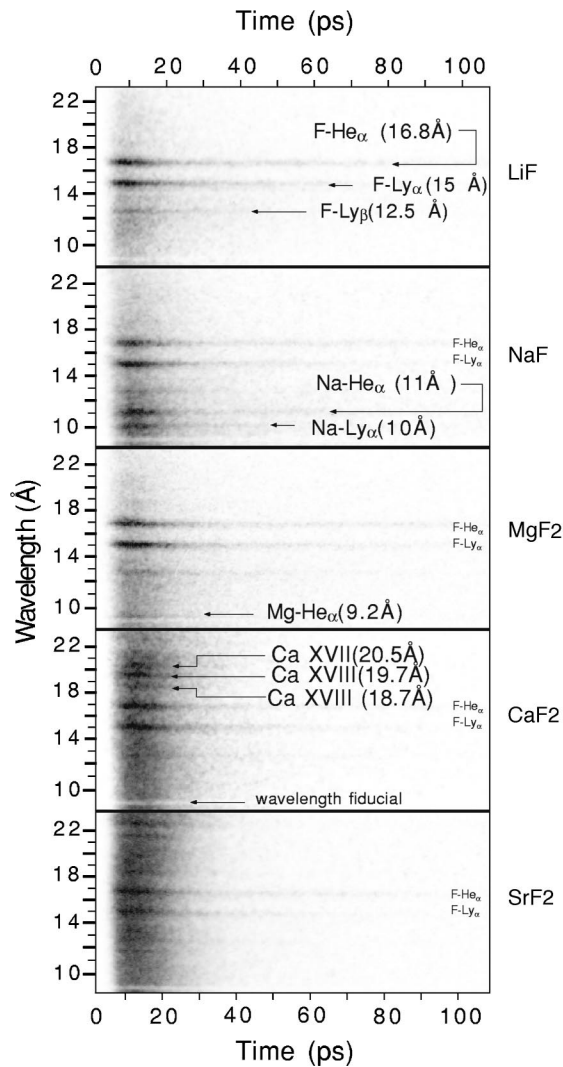
FIG. 2. Time-resolved spectra of the x-ray emission from LiF (top) to SrF$_2$ (bottom), in the range from 10 Å to 22 Å, obtained with a spectrometer equipped with a flat-field grazing incidence grating. The spectral and temporal resolution were 500 mÅ and 6 ps, respectively. Strong emission from bound-bound and free-bound transitions in H-like and He-like ions is visible. Short-lived continuum emission is also visible as a background emission due to bremsstrahlung (free-free) and recombination (free-bound).

is also visible, partially merged with the wavelength fiducial on the *blue* edge of the MgF$_2$ spectrum. Finally, Ca XVII and Ca XVIII lines are also visible in the case of the CaF$_2$ target.

The spectra of Fig. 2 have been processed to decouple the contribution of continuum emission from the lines. Since continuum emission varies slowly along the wavelength axis in comparison with line emission, the two components can be easily separated performing a one-dimensional (along the wavelength axis) spatial frequency domain analysis. An example of the result of this process is given in the plot of Fig. 3 which shows the lineout of the LiF spectrum taken at the peak of the emission and integrated over a temporal window of 20 ps, i.e., approximately twice the full width at half maximum (FWHM) of the laser pulse. The dotted line shows the original spectrum while the solid line shows the spectrum after removal of the background. The background only,
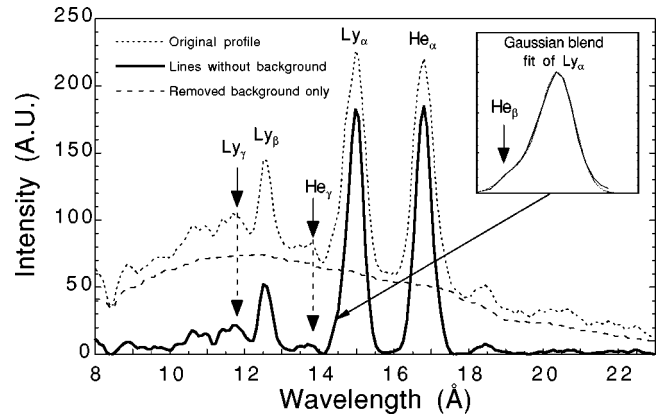
FIG. 3. Lineouts of the LiF target spectrum before (dotted line) and after (solid line) removal of the background continuum emission (see text). The background only, namely, the difference between the two spectra, is also plotted (dashed line). The lineouts were taken at the peak of emission intensity and integrated over 20 ps, that is, over 2 times the FWHM of the laser pulse. The clean spectrum shows the F-Ly$_\gamma$ ($1s$-$4p$) line at 12.0 Å as well as the F-He$_\gamma$ ($1s^2$-$1s4p$) line at 13.8 Å. In addition, the F-He$_\beta$ ($1s^2$-$1s3p$) line at 14.5 Å is also visible as a shoulderlike feature on the short-wavelength side of the F-Ly$_\gamma$ line. The inset shows the line profile of the F-Ly$_\alpha$ transition fitted with a blend of two Gaussian profiles that yields the relative intensities of the two components.

namely, the difference between the two spectra, is also plotted (dashed line) for comparison.

Wavelength calibration of this spectrum enables a more accurate identification of the emission lines arising from bound-bound transitions in H-like and He-like fluorine ions. Again, considering the LiF spectrum of Fig. 3, the F-Ly$_\gamma$ ($1s$-$4p$) transition and the F-He$_\gamma$ ($1s^2$-$1s4p$) transition are now more clearly visible. In addition, the F-He$_\beta$ ($1s^2$-$1s3p$) transition at 14.5 Å is just visible as a shoulderlike feature on the short-wavelength side of the F-Ly$_\alpha$ transition. For a more detailed analysis of this feature, the line profile of the F-Ly$_\alpha$ transition was fitted with a blend of two Gaussian profiles with the central wavelengths of the two lines fixed and the other coefficients (width and intensity) left as free parameters. The result of the fit is shown in the inset of Fig. 3 where the profile of the F-Ly$_\beta$ is transition compared with the fitting Gaussian blend. The position of the second Gaussian was found to be in agreement with the expected value of 14.5 Å within 5% and the FWHM of both Gaussian curves were found to be 0.45 Å, i.e., consistent with the FWHM of all the other lines. We note here that this value is much greater that the actual line width and is mainly due to a combination of instrumental and source-size effects and can be assumed as the overall spectral resolution of our spectrometer and streak-camera system.

IV. MODELING THE SPECTRA

Before we proceed with the comparison of the spectra obtained from different fluorine compounds, we analyze the spectra of Fig. 2 to obtain information on the physical properties of the source plasma and, in particular, on the electron temperature and density at the peak of the laser pulse. In fact, these quantities are related to line intensity ratios by means of plasma equilibrium processes and atomic physics proper-

TABLE I. Line intensity ratios and electron temperatures at the peak of the emission for the five types of target.

Target	LiF	NaF	MgF$_2$	CaF$_2$	SrF$_2$
Ly$_\alpha$/He$_\alpha$ ($\pm 10\%$)	0.94	1.10	1.05	0.97	0.84
Temperature (eV)	186–194	192–216	191–203	187–197	183–187

ties. Numerical simulations have been performed to calculate the line intensity ratios for a given set of hydrodynamic variables and for collisional-radiative equilibrium [15]. Additional information concerning the hydrodynamic properties of the plasma was obtained by numerical simulations performed with the one-dimensional (1D) Lagrangian hydrocode MEDUSA [16]. The code was used to estimate temperature and density profiles during the laser pulse. Plasma opacity effects were included by assuming propagation of x rays in a uniform plasma of 10 μm length. This plasma length was chosen taking into account that (i) the line of sight of the spectrometer (see Fig. 1) is basically parallel to the longitudinal plasma expansion direction (target normal) and (ii) the longitudinal plasma extent is set by the density scale length at the critical density which was measured [5] to be 10 μm. Finally, the spectral resolution of our spectra was also taken into account by convoluting the detailed spectrum with a 0.45 Å FWHM Gaussian profile.

The Ly$_\alpha$ to He$_\alpha$ intensity ratio $I_{\mathrm{Ly}_\alpha}/I_{\mathrm{He}_\alpha}$, taken at the peak of the laser pulse for all the spectra of Fig. 2 is shown in Table. I. As we can see, the ratio is close to unity for the available range of mean atomic number of the targets and is maximum for medium-Z targets (NaF and MgF$_2$). Now we compare these values with the values expected from numerical simulations. The plot of Fig. 4 shows $I_{\mathrm{Ly}_\alpha}/I_{\mathrm{He}_\alpha}$ as a function of the electron temperature, calculated for two different densities of 10^{22} and 10^{23} cm^{-3}. Within this density range and for $I_{\mathrm{Ly}_\alpha}/I_{\mathrm{He}_\alpha}=1$ the temperature falls in the range between 190 and 200 eV. Table. I shows the electron temperatures at the peak of the pulse for all the spectra of Fig. 2, as obtained from the plot of Fig. 4 for the two values of the electron density. As we can see, the small variations of the experimental ratios with the mean atomic number of the target result in slightly lower peak electron temperatures for lower- and higher-Z targets.
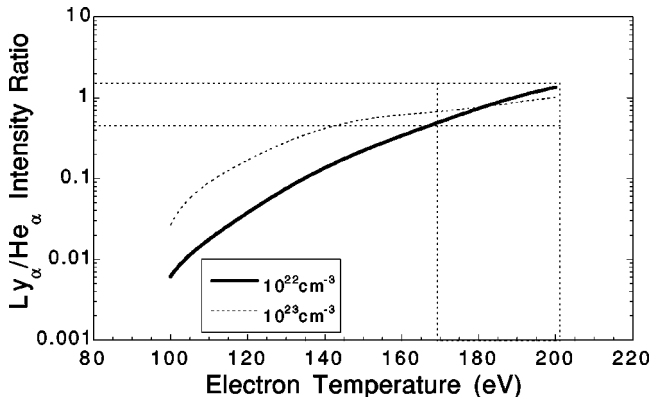
According to the plot of Fig. 4, higher densities tend to give the same ratios for higher temperatures. This may lead to slightly overestimating the temperature if a large fraction of the detected radiation originates from the higher-than-critical density regions. These circumstances may only occur in the early phase of the interaction, before the plasma scale length at the critical density has become sufficiently large to allow substantial collisional absorption. This plasma start-up phase is likely to last for a few picoseconds and anyway much less than the pulse duration. Such an effect has indeed been observed [5] at higher laser intensities on Al targets. However, in the experiment described here, due to the lower laser intensity, the overdense plasma region remains relatively cold (<100 eV) and very little He-like and H-like ions are generated. This is consistent with the predictions of hydrodynamic simulations as shown by the plots of Fig. 5 which give the temperature-density plots for three times close to the peak of the laser pulse. According to these plots, the density characterized by a given electron temperature decreases rapidly after the peak of the pulse and regions of sufficiently hot plasma (>100 eV) only exist at densities below 4×10^{22} cm^{-3}. We also observe here that no significant dielectronic satellite emission was detected in our spectra. According to atomic physics simulations, this implies that the electron density must be smaller than 5×10^{22} cm^{-3}.

Therefore, we conclude that, except at the very beginning of the emission, the density at which the dominant fraction of the detected emission occurs must not exceed a few times 10^{22} cm^{-3}.

The values of electron density, electron temperature, and plasma size obtained above, which are typical of all the spec-

FIG. 4. Calculated dependence of the Ly$_\alpha$ to He$_\alpha$ intensity ratio as a function of the electron temperature for two different densities of 10^{22} and 10^{23} cm^{-3} as obtained from the hydrocode MEDUSA.
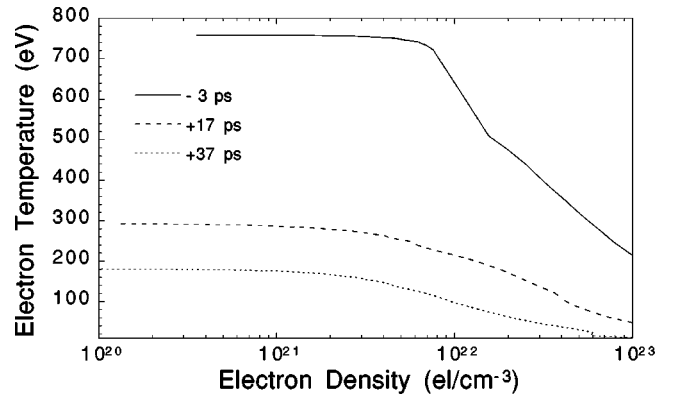
FIG. 5. Temporal evolution of the plasma temperature-density profile calculated using 1D hydrodynamic numerical simulations. Each curve identifies the densities and temperatures existing in the plasma profile at a given time. The 12 ps (FWHM) laser pulse peaks at +3 ps. The unheated target in this plot is represented by a single point at the simulation start-up temperature (1 eV) and at the solid density of the material ($n_e = 1.3 \times 10^{23}$ cm^{-3}).
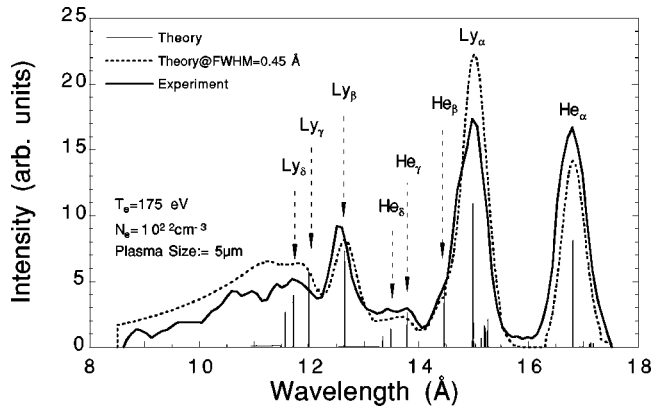
FIG. 6. Comparison between the experimental spectrum (solid line) and the spectrum calculated (dashed line) by the code SPECTRA for a 10-μm-thick plasma at an electron temperature of 180 eV and a density of 1.5×10^{22} cm^{-3} after convolution with a 0.45 Å FWHM Gaussian function to account for the spectrometer resolution. The original, unconvoluted spectrum is also shown for comparison.

tra of Fig. 2 at the peak of the laser pulse, were chosen to produce a synthetic spectrum using the atomic physics code SPECTRA. The resulting spectrum was then convoluted with a 0.45 Å FWHM Gaussian function to account for the experimental spectral resolution. A comparison between the synthetic spectrum and the experimental spectrum of Fig. 3 is shown in Fig. 6. Besides minor differences in the relative intensities of lines, likely to be due to spatial integration effects along the line of sight of the spectrometer, there is an overall good agreement between the calculated spectrum and the experimental one. In particular, the unresolved higher-series members (He$_\gamma$, He$_\delta$, Ly$_\gamma$, etc.) and the recombination continuum are well reproduced by the calculation.

V. EMISSION HISTORY: GENERAL PROPERTIES

The temporal evolution of the emission line intensity was obtained from the spectra of Fig. 2 by integrating the intensity over the whole linewidth. In general, three separate stages can be identified in the temporal evolution. A fast rise of the fluorine emission occurs early during the interaction and the maximum is reached at approximately 10 ps which corresponds to the peak of the laser pulse. This rapid response requires that ionization and excitation processes are fast compared to the rise time of the laser pulse. Indeed, calculations performed in analogous experimental conditions [11] show that in the case of low-Z atoms ($\leqslant 10$), ionization times are of the order of a picosecond or less while excitation and radiative decay times are even faster. Therefore in the case of fluorine this condition should be fully satisfied. The maximum of emission is then followed by a rapid fall of the intensity for ≈ 15 ps and by a long-term decay stage until the radiation goes below the detection level.

The first two stages of emission, up to ≈ 25 ps, take place while the laser pulse is still on and the temporal properties of the emission intensity are therefore influenced by the rate of laser energy input as well as by a combination of hydrodynamic and atomic physics effects. In contrast, during the third stage, no laser radiation is present and the decay rate of the emission intensity is determined solely by hydrodynamic

and atomic physics effects. It is interesting to observe that in the case of the LiF target ($\bar{Z}=6$), this long-term decay has a characteristic time of 39 ± 4 ps. This value is consistent with that obtained in the experiment of Ref. [9] where plasma was produced by laser irradiation of a carbon target ($Z=6$). In that case the decay time of the C-He$_\alpha$ line was measured to be 32 ± 5 ps.

We now compare the temporal behavior of the emission intensity of the same lines for the different spectra of Fig. 2 originating from plasmas of different mean atomic number. The plots of Figs. 7(a) and 7(b) show the temporal dependence of the He$_\alpha$ and the Ly$_\alpha$ line intensities from the peak of the emission to approximately 100 ps. The data were fitted with a power law (dotted curve) and the values of the exponent of the best fit are shown for each curve. As we can see, both sets of curves show a clear increase of the exponent with the atomic number of the alkali component of the target indicating a faster decay of the emission intensity. We also observe a sort of saturation effect in SrF$_2$ which shows a decay rate similar to that of CaF$_2$.

The general behavior can be found in both sets of Ly$_\alpha$ and He$_\alpha$ lines with the Ly$_\alpha$ set showing consistently higher exponents than in the case of the He$_\alpha$ set. More important, if we take the Ly$_\alpha$ to He$_\alpha$ intensity ratios as obtained from the fits of Fig. 7 and using the plot of Fig. 4 to convert ratios in temperatures, we find the temporal evolution of the electron temperature as shown by the plots of Fig. 8. These curves clearly show the effect of faster cooling rates in higher-Z targets.

The key question now is whether this dependence is an intrinsic property of the plasma or is a consequence of different initial conditions, arising, for example, from different laser coupling efficiencies. First of all we point out that in our case we are comparing the effect of relatively small atomic numbers. As shown in the plot of Fig. 8, higher peak temperatures are obtained for medium-Z targets. Higher initial temperatures should give rise to a faster expansion and a more efficient cooling of the plasma with consequent faster decay of the emission. Our data show no correlation between the peak temperature and the cooling rates. On the contrary, higher cooling rates have been found for higher-Z targets, for which lower temperatures have been observed. Therefore it is reasonable to assume that the observed effect is due to a characteristic property of the plasma rather than to coupling conditions. Radiation losses are clearly the primary candidate to explain the observed effects.

Depending on the atomic number of the species present in a plasma, the dominant contribution to radiation losses can come from line emission or continuum emission. In our case, in the spectral range from 8 to 24 Å, continuum emission largely dominates, its intensity being 3 (LiF) to 6 (SrF$_2$) times larger than line emission intensity. In these circumstances, the power radiated by the plasma will depend upon its charge state. Although a detailed evaluation of the actual charge state is a difficult task and is beyond the aim of this work, some important conclusions can be made starting from simple considerations. First of all it is reasonable to assume that the mean charge state tends to increase with the mean atomic number of the target. In particular, in the case of low- and medium-Z targets (LiF, NaF, and MgF$_2$), according to atomic physics simulations the alkali species is expected to
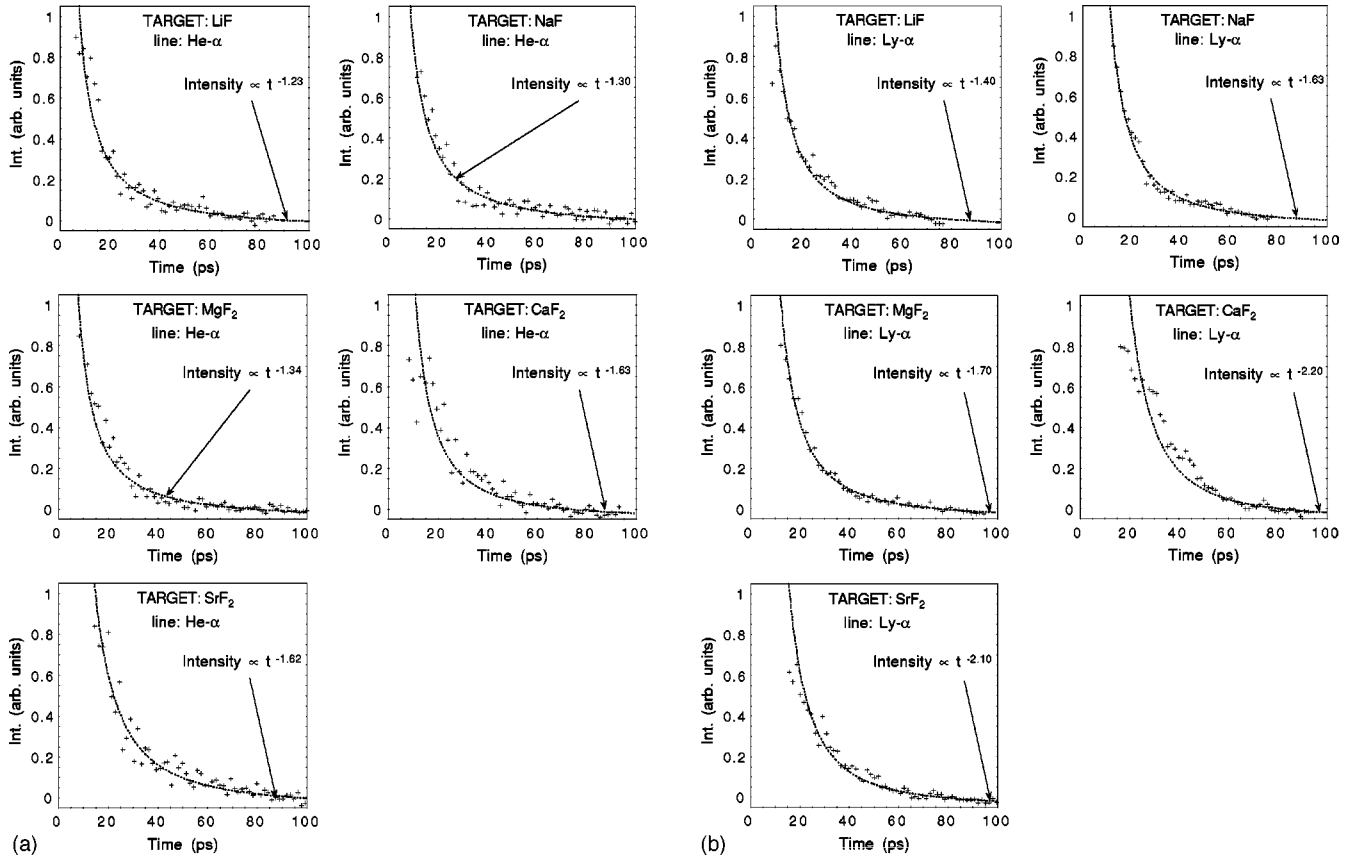
FIG. 7. Temporal dependence of (a) He_α and (b) Ly_α line intensities from the peak of the emission to approximately 100 ps. The experimental data (crosses), taken from the spectra of Fig. 2 sampling the intensity of emission lines every two picoseconds, were fitted with a power law (dotted curve) assuming an experimental error of 20%. The values of the exponent of the best fit are shown for each curve.

be almost fully ionized. Therefore, the mean charge state will be close to the mean atomic number of the targets. Consequently, the mean charge states of NaF and MgF_2 are expected to be very similar and substantially greater than that of LiF. In the case of CaF_2, the presence of Ca^{16+} (Be-like) and F^{8+} (H-like) in the CaF_2 spectrum of Fig. 2 suggests that a mean charge state at least 2 times higher than that of the LiF target should be achieved. Finally, since Ca in CaF_2 plasma is only partially ionized (approximately 16+), a similar ionization should occur for Sr with only minor changes

FIG. 8. Temporal evolution of the electron temperature as obtained from the Ly_α to He_α intensity ratios of the spectra of Fig. 2 using the calculations of the atomic physics code given in Fig. 4.

due to the differences in the detailed electronic structure of the two atoms. Therefore SrF_2 is expected to have a charge state similar to that of CaF_2.

According to these observations, radiation cooling effects are expected to increase going from LiF to NaF and from MgF_2 to CaF_2, while going from NaF to MgF_2 and from CaF_2 to SrF_2 no large variations should be observed. This behavior explains the features pointed out when describing the plots of Fig. 7 where comparable decay constants of both Ly_α and He_α lines were found for NaF and MgF_2 and for CaF_2 and SrF_2. This correlation between the estimated charge states of the plasma and the measured cooling constants strongly suggests that radiation loss is the mechanism responsible for the observed faster cooling in higher-Z targets.

VI. CONCLUSIONS

We have used time-resolved x-ray spectroscopy to study the temporal evolution of plasmas produced by high-contrast picosecond laser irradiation of solid targets consisting of fluorine salts of different mean atomic number. The main spectral features including fluorine resonance lines and continuum emission at the peak of emission have been compared to hydrodynamic and atomic physics simulations and show good agreement with the calculated emission for peak plasma electron temperatures ranging from 185 to 200 eV

and an electron density close to the critical density of 1.5 $\times 10^{22}$ cm^{-3}. It was shown that the temporal evolution of the intensity of both He-like and H-like main resonance lines exhibits a faster decay for higher-Z targets as a result of a faster cooling of the plasma. This effect has been explained in terms of radiation cooling in higher-Z targets.

[1] M. Murnane and H.D. Kapteyn, Phys. Fluids A **3**, 2409 (1991).

[2] K. Eidmann and W. Schwanda, Laser Part. Beams **9**, 551 (1991).

[3] D. Giulietti and L.A. Gizzi, Riv. Nuovo Cimento **21**, 1 (1999).

[4] R.C. Elton, *X-ray Lasers* (Academic, San Diego, 1990).

[5] D. Riley, L.A. Gizzi, A. MacKinnon, S.M. Viana, and O. Willi, Phys. Rev. E **48**, 4855 (1993).

[6] D. Riley, L.A. Gizzi, F.Y. Khattak, A.J. Mackinnon, S.M. Viana, and O. Willi, Phys. Rev. Lett. **69**, 3739 (1992).

[7] L.A. Gizzi, A.J. Mackinnon, D. Riley, S.M. Viana, and O. Willi, Laser Part. Beams **13**, 511 (1995).

[8] C.Y. Cote, J.C. Kieffer, and O. Peyrusse, Phys. Rev. E **56**, 992 (1997).

[9] C. Wülker, W. Theobald, F.P. Schäfer, and J.S. Bakos, Phys. Rev. E **50**, 4920 (1994).

[10] J.R. Barr, N. Everall, C. Hooker, I. Ross, M. Shaw, and W. Toner, Opt. Commun. **60**, 127 (1988).

[11] L.A. Gizzi, Ph.D. thesis, Imperial College of Science, Technology and Medicine, University of London, 1994 (unpublished).

[12] D. Strickland and G. Morou, Opt. Commun. **54**, 219 (1985).

[13] D. Giulietti, L.A. Gizzi, A. Giulietti, A. Macchi, and D. Teychenn, Phys. Rev. Lett. **79**, 3194 (1997).

[14] T. Kita, T. Haroda, N. Nakano, and H. Kuroda, Appl. Opt. **22**, 512 (1983).

[15] R.W. Lee, B.L. Whitten, and R.E. Stout II, J. Quant. Spectrosc. Radiat. Transf. **32**, 91 (1984).

[16] J.P. Christiansen, D.E.T.F. Ashby, and K.V. Roberts, Comput. Phys. Commun. **7**, 271 (1974); P.A. Rodgers, A.M. Rogoyski, and S.J. Rose (unpublished).